CHEMISTRY OF MATERIALS

Article

pubs.acs.org/cm

Evidence for near-Surface NiOOH Species in Solution-Processed NiO_x Selective Interlayer Materials: Impact on Energetics and the Performance of Polymer Bulk Heterojunction Photovoltaics

Erin L. Ratcliff,*,† Jens Meyer,‡ K. Xerxes Steirer,§ Andres Garcia,§ Joseph J. Berry,§ David S. Ginley,§ Dana C. Olson,§ Antoine Kahn,‡ and Neal R. Armstrong*,†

†Department of Chemistry, University of Arizona, Tucson, Arizona 85721, United States

‡Department of Electrical Engineering, Princeton University, Princeton, New Jersey 08544, United States

§National Renewable Energy Laboratory, Golden, Colorado 80401, United States

Supporting Information

ABSTRACT: The characterization and implementation of solution-processed, wide bandgap nickel oxide (NiO_x) hole-selective interlayer materials used in bulk-heterojunction (BHJ) organic photovoltaics (OPVs) are discussed. The surface electrical properties and charge selectivity of these thin films are strongly dependent upon the surface chemistry, band edge energies, and midgap state concentrations, as dictated by the ambient conditions and film pretreatments. Surface states were correlated with standards for nickel oxide, hydroxide, and oxyhydroxide components, as determined using monochromatic X-ray photoelectron spectroscopy. Ultraviolet and inverse photoemission spectroscopy measurements show changes in the surface chemistries directly impact the valence band energies. O_2-plasma treatment of the as-deposited NiO_x films was found to introduce the dipolar surface species nickel oxyhydroxide (NiOOH), rather than the p-dopant Ni_2O_3, resulting in an increase of the electrical band gap energy for the near-surface region from 3.1 to 3.6 eV via a vacuum level shift. Electron blocking properties of the as-deposited and O_2-plasma treated NiO_x films are compared using both electron-only and BHJ devices. O_2-plasma-treated NiO_x interlayers produce electron-only devices with lower leakage current and increased turn on voltages. The differences in behavior of the different pretreated interlayers appears to arise from differences in local density of states that comprise the valence band of the NiO_x interlayers and changes to the band gap energy, which influence their hole-selectivity. The presence of NiOOH states in these NiO_x films and the resultant chemical reactions at the oxide/organic interfaces in OPVs is predicted to play a significant role in controlling OPV device efficiency and lifetime.

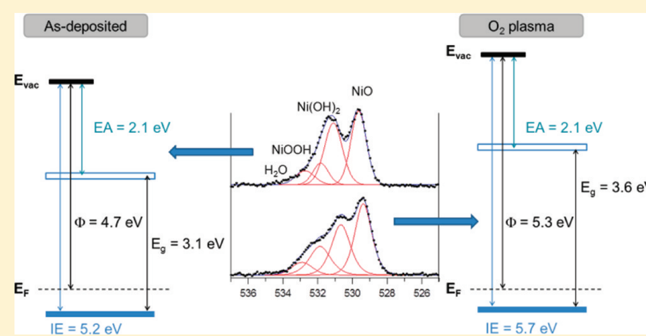

KEYWORDS: *nickel oxide, interlayer, selective contact, organic solar cell, OPV, photoemission spectroscopy, UPS, IPES, XPS*

INTRODUCTION

Polymer–fullerene blends, or bulk heterojunctions (BHJs), represent the most promising architecture in organic photovoltaics (OPVs) for increasing photocurrent yield and overall energy conversion efficiencies.[1−8] However, the extensive intermixing of donor and acceptor phases may result in both entities being in simultaneous contact with both hole-harvesting and electron-harvesting electrodes.[4,7−11] Charge recombination events can therefore dominate at the contacts, resulting in a significant loss of power conversion efficiency, typically manifested in reduced open circuit voltages (V_{OC}).[7,9−24]

To minimize contact localized recombination, charge-selective interlayers are added between both hole- and electron-harvesting electrodes and the photoactive layer to control energetic barriers to charge harvesting and increase the selectivity of the contact. Such functionality of an interlayer is often described as charge selectivity, with a proposed preferential harvesting of specific charge carriers (either holes or electrons) at the appropriate contact.[8,9,25−29] Recent studies on OPV materials and devices suggest that interlayer materials can establish both thermodynamic constraints on charge collection (based on the ionization energy (IE) and electron affinity (EA) of the interlayer material relative to the hole and electron transport energies of the active layer in the OPV)[8,30] and kinetic constraints (where the interlayer simply enhances the rate of harvesting of one charge carrier over the other).[7] The use of interlayers at electrode/active layer interfaces improves the current−voltage rectification of the device[9,26,31−35] and is essential to balance rates of hole and electron harvesting at both contacting electrodes.[18,36,37] There have been numerous selective contacts developed to date,

Received: August 5, 2011
Revised: October 13, 2011
Published: October 26, 2011

© 2011 American Chemical Society

dx.doi.org/10.1021/cm202296p | Chem. Mater. 2011, 23, 4988−5000

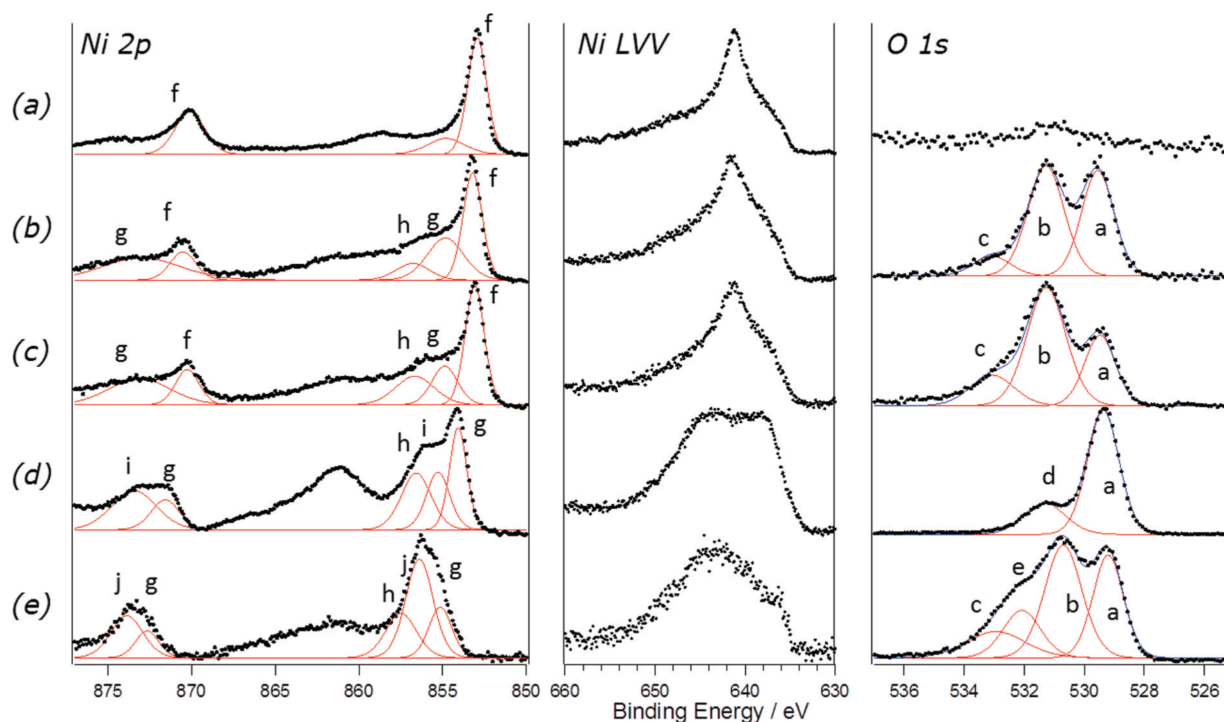

Figure 1. Ni 2p, Ni Auger (LVV), and O 1s spectra for Ni foil controls. From top to bottom: (a) Ar ion sputtered Ni metal, (b) Ar ion sputtered Ni metal exposed to O_2 gas for 10 min, (c) Ar ion sputtered Ni metal exposed to ambient for 10 min, (d) Ni foil heated to 500 °C in the presence of O_2, (e) Ni foil electrochemically oxidized in 1 M KOH for 120 s under a N_2 blanket. Raw data are given by (●) and with fitted components (red lines) and the net fit (blue lines). Peaks for the Ni 2p spectra are added only to guide the eye to changes in spectral shape discussed in the text and do not represent full component analysis.

including polymers, doped small molecules, and metal oxides.[7,8] How these interlayers operate and their impact on interfacial dynamics of BHJs continues to be a significant area of study.

Metal oxides are a recently introduced class of materials for either hole- or electron- selective interlayer materials.[8,38−43] Certain p-type metal oxides, such as nickel oxide, are suggested to be hole-selective due to a combination of two properties: (i) an energy match of the oxide valence band energy (E_{VB}) to the hole transport level or highest occupied molecular orbital (HOMO) of the donor and (ii) a large bandgap, yielding an oxide conduction band (E_{CB}) closer to the vacuum level than the lowest unoccupied molecular orbital (LUMO) of either the donor or the acceptor, a property necessary for thermodynamic electron blocking.[8,38] Nickel oxide (NiO_x) thin films on indium tin oxide ITO have been utilized to enhance hole injection in light emitting diodes (LEDs), resulting in a decrease in turn on voltages.[44,45] The functionality of NiO_x as a contact interlayer in quantum dot-based LEDs was proposed by Bulovic, Bawendi and co-workers;[46−48] the wide band gap (~3 eV) and deep valence band energy was hypothesized to align with the hole transport level of various donor polymers.[38,39,49−53] A more detailed explanation on the origin of the band gap in stoichiometric NiO is provided in the Supporting Information. NiO_x interfacial layers have been fabricated by various methods for OPV applications, including pulse laser deposition,[38,39,54] sputtering,[49,52,53,55] oxygen plasma treatment of metallic nickel,[56] and processing via spin-casting from solution precursors.[50,51] Inclusion of NiO_x interlayers have recently been demonstrated to improve the efficiency of several types of BHJ OPVs and improve the lifetime of these devices relative to OPVs created with doped poly(thiophene) interlayers (poly(3,4-ethylenedioxythiophene) poly(styrenesulfonate) or PEDOT:PSS).[38,5057] Recently, Irwin and co-workers have also demonstrated that NiO_x interlayers deposited over ITO electrodes improved the electrical homogeneity of that contact.[39]

Despite all of the appealing energetic qualities for inclusion in OPVs, NiO_x materials are known to demonstrate complex surface chemistries and are susceptible to hydration in ambient conditions.[58,59] Doping of NiO has been recently summarized,[60] with NiO shown to p-dope (with holes) through two mechanisms. The first is the introduction of intrinsic defects, which has been attributed to the production of Ni^{3+} centers.[60−65] However, it is energetically more favorable that the charge compensation is derived from O^{1-} ions or ligand holes.[66] The second method for hole doping is the substitutional replacement of Ni^{2+} with Li^{+}, again pointing to the creation of O^{1-} ions in order to maintain charge neutrality.[60] Ni^{3+}, however, is known to be a strong oxidizing agent,[67] which should dramatically impact the interfacial chemical interactions between a Ni^{3+} containing material and an active layer with electron-donating polymers or small molecules. Recent reports of BHJ OPVs formed with NiO_x interlayers have alluded to Fermi level pinning at the NiO_x/donor-polymer interface, promoting bulk-limited contacts for improved hole extraction.[50] Solution-processed NiO_x (s-NiO_x) is especially interesting for scalable OPV fabrication, but attention must be paid during processing to various surface reactions which change the properties of the NiO_x interlayer and the oxide/organic interface. It is as yet unclear how the chemical reactivity of NiO_x films and the distribution of surface states (with complex compositions) are altered by post-deposition treatments such as O_2 plasma activation. Such pretreatments can influence the surface chemistry of these interlayers and ultimately OPV

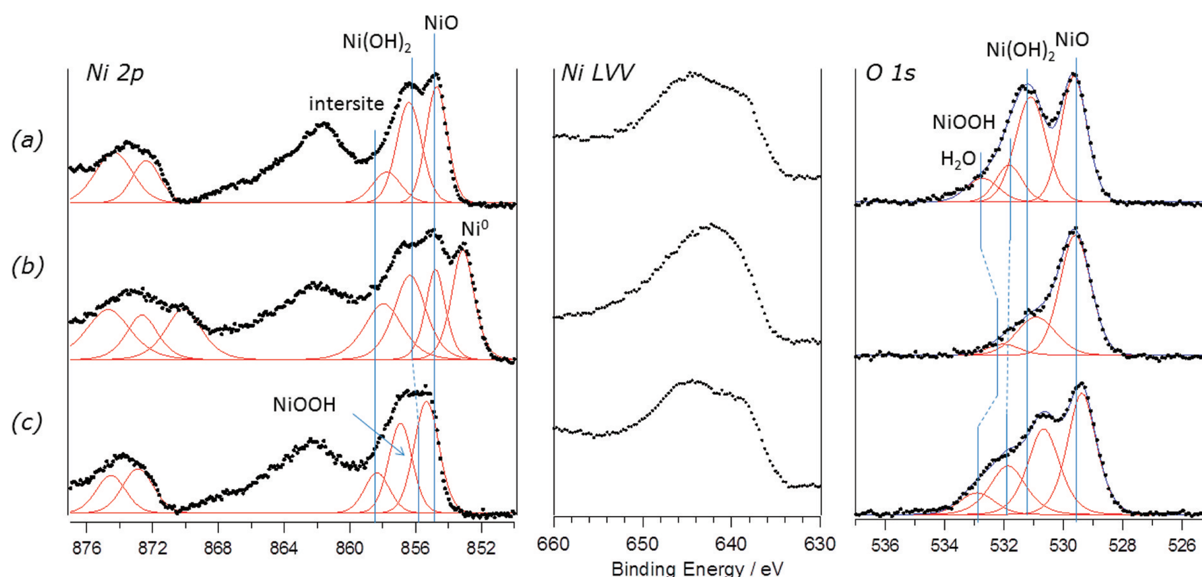

Figure 2. Ni 2p, Ni Auger (LVV), and O 1s spectra the pretreatments of s-NiOx films. (a) "As-deposited" NiOx, (b) Ar ion-sputtered NiOx, and (c) O_2-plasma treated NiOx. Raw data is given by (●) and with fitted components (red lines) and the net fit (blue lines). Peaks for the Ni 2p spectra are added only to guide the eye to changes in spectral shape discussed in the text and do not represent sufficient component analysis. An expanded plot of the Ni Auger peaks is provided in the Supporting Information.

device performance. This manuscript represents the first in a series of characterizations of solution-processed NiO_x/organic interfaces and how plasma treatment of the oxide prior to device preparation affects interfacial charge transfer rates relevant to OPV platforms.

The surface chemistries, electrical properties, and interfacial states of as-deposited and pretreated s-NiO_x films are presented below, with the intended functionality as a hole-selective contact: (i) "as-deposited" AD-s-NiO_x films; (ii) AD-s-NiO_x following Ar ion-sputtering ("Ar-s-NiO_x"); and (iii) AD-s-NiO_x films following O_2 plasma treatment ("OP-s-NiO_x"). The paper is divided into three sections. The initial focus is on the characterization of various nickel metal and nickel oxide (and oxy-hydroxide) standards using monochromatic X-ray photoemission spectroscopy (XPS), which guides interpretation of the surface composition of AD-, Ar-, and OP-s-NiO_x interlayer films. In the second section, changes in near-surface composition are correlated to the observed changes in valence band energies (measured using ultraviolet photoemission spectroscopy, UPS) and conduction band energies (evaluated with inverse photoemission spectroscopy, IPES). In the final section, the contact selectivity for AD- and OP-s-NiO_x films is evaluated using electron only devices, designed to inject electrons from either the top or bottom contacts and BHJ OPVs, where the current density−voltage (J−V) properties and device performance help to explain the electron blocking properties of s-NiO_x films.

■ RESULTS AND DISCUSSION

XPS of Metallic Nickel, Nickel Oxide Standards, and s-NiO_x Films. Standards for nickel metal and nickel oxide, selected to provide a broad spectrum of possible compositions of the s-NiO_x interlayer films, were created using a nickel metal foil and were prepared ex situ to mimic realistic solution-processing techniques, immediately prior to XPS/UPS/IPES characterization (Figure 1). These are compared with the photoemission spectra for three different s-NiO_x films (Figure 2) deposited on gold foils: (i) AD-s-NiO_x films, (ii) Ar-s-NiO_x films, and (iii) OP-s-NiO_x films a pretreatment confirmed to increase the efficiency of BHJ OPVs compared to AD-s-NiO_x.[50,51,54,57]

Figure 1 shows the O 1s and Ni 2p XPS spectra, and the X-ray induced LVV Ni Auger transition for various standard materials. These spectra are some of the highest-resolution XPS data obtained to date for nickel oxides, particularly for the O 1s region, and help provide insight into the composition of complex mixed nickel oxide films. The O 1s spectra in Figure 1 were fit using chemically reasonable and clearly resolved chemical components, while maintaining consistent fwhm for individual peaks.

Nickel has a predominant oxidation state of +2, but can also be found with oxidation states ranging from +1 to +4.[67] Metallic nickel is known to be highly reactive with ambient environments, with approximately three monolayers of NiO and/or $Ni(OH)_2$ forming spontaneously on atomically clean nickel metal.[68] Higher oxidation state forms of nickel oxides include Ni_2O_3, Ni_3O_4, and NiO_2. In aqueous solutions, Ni^{2+} is the dominant species, although there is evidence for the existence of Ni^{3+} (a known oxidizing agent for water)[69,70] which might be present as well in solutions used to form NiO_x interlayer films (see below).

Clear assignments of the true oxidation state of nickel are complicated by the complexity of the Ni 2p spectrum.[71] Previous XPS analyses of nickel oxides show that there is strong overlap between the peaks for Ni^{2+} and Ni^{3+} in Ni 2p photoemission spectra, while metallic nickel can be clearly resolved.[72] The complex Ni 2p XPS spectrum for stoichiometric NiO is often described using a core metal d-electron state (c) and the ligand oxygen p-electron (L) notation, with the main cd^9L photoemission peak at a binding energy (BE) of ∼854.6 eV accompanied by a broad satellite peak at ∼861.7 eV (fwhm ∼6 eV), the later stemming from the unscreened cd^8 final state component.[73] An additional shoulder to the cd^9L component appears near 856.1 eV, which cannot be modeled with cluster calculations (i.e., a single octahedral NiO_6 cluster).[74] This significant shoulder peak has often been

Table 1. Binding Energies for O 1s Components, Reference Energies for Ni 2p Spectra, and Auger Parameters (α) for Figure 1[a]

	O 1s	% composition	Ni $2p_{3/2}$	Ni $2p_{1/2}$	Ni $2p_{1/2}$-Ni $2p_{3/2}$	Ni $2p_{3/2}$ intersite[i]	Ni $2p_{3/2}$ satellite	α'	α''
Ni metal Ar^+ sputtered	N/A	N/A	852.9[g]	870.1[g]	17.2	854.8	858.5	1698.4	N/A
Ni metal O_2 exposure	529.6[b]	41.9	853.1[g]	870.4[g]	17.3	856.7	860.0	1698.3	N/A
	531.3[c]	48.9	854.7[h]	872.9[h]	18.2			1699.9	N/A
	533.1[d]	9.3							
Ni metal ambient exposure	529.5[b]	26.8	853.1[g]	870.3[g]	17.2	856.7	860.3	1698.4	N/A
	531.3[c]	56.8	854.9[h]	873.1[h]	18.2			1700.2	N/A
	533.1[d]	16.4							
Ni metal heated 500 °C in ambient	529.4[b]	75.1	854.1[h]	871.6[h]	17.5	856.6	861.2	1698.4	1702.2
	531.3[e]	24.9	855.3[j]	873.5[j]	18.2			1699.6	1703.4
Ni metal electrochemically oxidized	529.2[b]	29.4	855.2[h]	872.7[h]	17.5	857.5	861.6	1699.1	1705.2
	530.7[c]	39.5	856.4[k]	873.8[k]	17.4			1700.3	1706.4
	532.1[f]	16.7							
	532.9[d]	14.5							

[a] $\alpha' = KE_{Auger} + BE_{photoelectron}$; α'' uses the higher kinetic energy (lower binding energy) shoulder of the Auger peak. [b] O 1s component of NiO. [c] O 1s component of $Ni(OH)_2$. [d] O 1s from physisorbed H_2O. [e] O 1s from Ni_2O_3. [f] O 1s from NiOOH. [g] Metallic Ni character. [h] Ni 2p for NiO/$Ni(OH)_2$. [i] Ni $2p_{3/2\ intersite}$. [j] Ni 2p for Ni_2O_3. [k] Ni 2p for NiOOH.

associated with defects, including both Ni^{3+} and Ni^0 species.[75] Others have attributed this shoulder to nonlocal screening, which has been associated with oxygen atoms outside the octahedral NiO_6 cluster (neighboring octahedral NiO_6 units)[74,76] and confirmed with the use of alkali dopants.

Grosvenor et al,[77] and Biesinger et al.,[71,78] have recently concluded that the full Ni 2p photoemission envelope, for pure Ni^{2+} species (e.g., NiO or $Ni(OH)_2$) and pure Ni^{3+} species (e.g., γ-NiOOH) can be fit with a unique set of seven components, derived from the multiplet line shapes for free ions calculated by Gupta and Sen.[79,80] Mixtures of the two oxidation states therefore require fits for both Ni^{2+} and Ni^{3+} components, resulting in a fourteen-component fit for a binary system.[77,78] Because the NiO_x films in Figure 1 are clearly mixtures of different oxidation states of nickel, statistically unique line shapes were not obtainable with the inclusion of all components. Instead, Ni 2p data was fit using chemically reasonable and previously assigned peaks, which serve as a guide to changes in near-surface composition. These peaks can be correlated to one of the Ni standard states, or mixtures of those states. These studies establish a binding energy calibration table (Table 1) for various nickel oxide species in order to later evaluate the near-surface composition of s-NiO_x films.

Metallic Nickel. Figure 1a shows the spectra for the nickel foil, argon-ion sputtered under vacuum until O 1s and C 1s peaks fell below detection limits. The separation of the Ni $2p_{3/2}$ and Ni $2p_{1/2}$ is ~17.2 eV and the Auger parameter ($\alpha = KE_{Auger} + BE_{2p3/2\text{-}photoelectron}$) is 1698.4 eV and both measurements are consistent with values previously reported for Ni^0.[81,82] The Ni 2p peak at 852.9 eV has clear metallic character, as demonstrated by asymmetric tailing of the photoemission peak to higher binding energies; the formation of even a monolayer of oxide generally suppresses the energy loss processes governing asymmetric metallic line shapes.[83]

Ni^{2+} Species on Ni Foils Exposed to Ambient Gases. Ni^{2+} typically exists as either NiO or $Ni(OH)_2$, with the passivation of metallic nickel commonly described as a layer model of molecular NiO growth on the metal surface under a compact layer of $Ni(OH)_2$ in contact with ambient/solution environments.[69] NiO is formed via nucleation and lateral growth of oxide islands, resulting from a dissociative chemisorption reaction with oxygen.[68] Chemisorbed hydroxide radicals are hypothesized to form through the surface initiated dissociation of water, yielding the generally accepted NiO/$Ni(OH)_2$ model. $Ni(OH)_2$ species can be further categorized as hydrated α-$Ni(OH)_2$ and anhydrous β-$Ni(OH)_2$, the β-phase arises from the dehydration of the α-phase at temperatures above 240 °C.[67] Metallic Ni behaves as an electropositive metal and the oxidation of Ni to either NiO or $Ni(OH)_2$ proceeds with similar thermodynamic driving forces. It is therefore difficult to produce stoichiometric NiO under ambient conditions.[58] An effort was made to locally control the surface concentrations of NiO to $Ni(OH)_2$ species on the surface to systematically evaluate the binding energies of each.

Figure 1b,c show the spectra for the atomically clean nickel foil exposed for 10 min to either O_2 gas, first passed through a drying tube, or oxygen as a component of laboratory ambient conditions. The two O 1s peaks at ~529.6 and 531.3 eV are attributed to NiO and $Ni(OH)_2$ species, respectively. A third, higher binding energy component at ~533.1 eV is associated with bound waters of hydration.[71,75] The assignment of the $Ni(OH)_2$ species is verified by the increase in the higher binding energy O 1s component at ~531.3 eV, when comparing spectra for the nickel foil exposed to dry O_2 gas versus exposure to ambient conditions (Figures 1b,c). Using a higher photoemission takeoff angle (60°), and hence a more surface sensitive measurement, indicates this is predominantly a surface species. Further tailing at higher binding energies in the O 1s spectrum is evident, attributable to physisorbed or nondissociated water. There is also a possibility for residual decomposition products from thermodynamically unstable higher oxidation components (discussed below). High binding energies components are often associated with adsorption of carbonaceous species onto oxides but can be eliminated in this

dx.doi.org/10.1021/cm202296p | Chem. Mater. 2011, 23, 4988–5000

case since increased contributions from the high binding energy O 1s peak did not correspond with increasing C 1s peak area.

Coverages of both NiO and $Ni(OH)_2$ on metallic Ni are estimated to be at the monolayer scale,[68] and correspond with a shift of the Ni 2p peak to slightly higher binding energies (from 852.9 for the Ar ion sputtered Ni metal in Figure 1a, to 853.1 eV for Figure 1b,c) with little change in the shape of the nickel Auger peaks. For Figures 1b and 1C, the difference in the predominant, low binding energy, metallic components for Ni $2p_{3/2}$ and Ni $2p_{1/2}$ is still ∼17.3 eV, indicating residual metallic character. Aside from the metallic Ni 2p regions, both the dry O_2 and the ambient exposed Ni foils have additional contributions that can be correlated with the two lower binding energy peaks in the O 1s spectra. The dry O_2 exposed sample spectrum is consistent with NiO (Figure 1b) having component peaks at ∼854.7 and 856.7 eV for the Ni $2p_{3/2}$ and a broad peak at ∼872.9 eV for the Ni $2p_{1/2}$, with the larger contribution from the 854.7 eV component. The separation between the Ni $2p_{3/2}$ NiO and the Ni $2p_{1/2}$ NiO is ∼18.2 eV. In contrast, the Ni $2p_{3/2}$ spectrum for the Ni foil exposed to ambient (Figure 1c) has two components at 854.9 and 856.7 eV, both of which are shifted to higher binding energies compared to the O_2-exposed sample (Figure 1b), and a Ni $2p_{1/2}$ component at ∼873.1 eV, resulting in a Ni $2p_{1/2}$−Ni $2p_{3/2}$ binding energy separation of ∼18.2 eV. The net contribution for the 854.9 eV component is higher for the ambient exposed sample, suggesting there is some overlap between the satellite attributed to nonlocal screening and the hydroxide component, seen in the O 1s spectra.

Ni_2O_3 Formed at High Process Temperatures. Figure 1d shows the spectra for the Ar ion sputtered Ni film subsequently exposed to oxygen at 500 °C. At this temperature, there should be no adsorbed water and any hydroxylated species should be converted to the oxide.[67] The presence of NiO can be seen in the dominant peak in the O 1s spectrum at ∼529.4 eV, a slightly lower binding energy than the foils exposed to ambient or dry O_2. Also, there is a high binding energy peak (∼531.3 eV) that is 1.8 eV from the NiO O 1s peak, with a more pronounced degree of tailing. Previous reports have suggested that, at elevated temperatures, there is an evolution in oxide formation including transitions through nonstoichiometric states, which correlates with the evolution of a higher binding energy O 1s component shifted by ∼1.8 eV, attributed to Ni_2O_3 defects.[55,68,84−87] The presence of Ni_2O_3 is also confirmed in the Ni 2p spectrum, where the Ni 2p peak has the predominant third component near 855.3 eV.[72,85] Literature XPS results for Li^+ doped NiO, a complementary p-doped nickel oxide system, demonstrated a shift to lower binding energy (∼0.4 eV) in the O 1s spectrum as the concentration of Li^+ was increased.[60] Changes in the Ni 2p line shape were also observed, with a decrease in the proposed NiO peak at ∼855 eV relative to the interstate peak at ∼856.7, although no direct correlations were discussed.[60] The conclusion of partial conversion to Ni_2O_3 seems reasonable, since at 500 °C, full dehydration/dehydroxylation of the film is expected. There is also a clear difference in the Figure 1d Ni Auger spectrum, when compared with Figures 1a-c, with two distinct peaks indicating the partial conversion of NiO to Ni_2O_3. This is further supported by the O 1s spectrum where there are multiple domains within the film that are representative of unique oxidation states. From these results there are two clearly different oxidation states of nickel present in these thin films, namely Ni^{2+} and Ni^{3+}. It is important to note, however, that there is still some disagreement in the literature regarding the speciation of nickel in "doped" NiO, where, for example, Adler et al. have suggested that the energetic formation of Ni^{3+} is unfavorable, and that charge compensation should occur with O^- ions, or ligand holes.[66] The difference between this form of high-temperature processed nickel oxide and the s-NiOx films discussed below is nevertheless clear.

Electrochemically Grown NiOOH. Aside from a Ni_2O_3 species, higher order oxidation states of nickel can also be formed by the further oxidation of nickel hydroxides summarized by the following simplified reaction[67]

$$Ni(OH)_2 \rightleftarrows NiOOH + H^+ + e^-$$

The presence of oxy-hydroxide intermediates (NiOOH) have been suggested by Bockris et al. and are associated with the lower thermodynamic potential for oxidation of water molecule to H_2O_2 and oxygen ($E^0_{H2O2/H2O} \approx 1.77$ V; $E°_{O2/H2O2} = 0.68$ V) versus the oxidation of water to OH radicals to oxygen ($E^0_{OH/H2O} = 2.8$ V; $E°_{O2/H2O} = 2.4$ V).[58,70,88] Because of this lower thermodynamic potential, it was hypothesized that NiOOH species may be created upon O_2-plasma etching of the s-NiO_x films in Figure 2. Because of the known reactivity of Ni^{3+} species, the sample was immersed under potential control, quickly rinsed, and immediately loaded into a vacuum while under argon gas.

The XPS data in Figure 1e are consistent with previous photoemission data for NiOOH films,[77,78,89] and show unique O 1s, Ni 2p and LVV Auger peaks when compared to the Ni_2O_3 standard shown in Figure 1d. The O 1s spectrum is fit with four O 1s peaks, including the peak for NiO at ∼529.21 eV and the peak for $Ni(OH)_2$ at ∼530.7 eV both of which have shifted to slightly lower binding energies than the samples in Figure 1a−d, consistent with previous reports of NiOOH characterization.[89] A new component at ∼532.1 eV is observed associated with the oxyhydroxide, NiOOH. Finally, the highest binding energy component in Figure 1e is attributed to physisorbed water at ∼532.9 eV.[71,75]

The Ni 2p spectrum in the NiOOH film (Figure 1e) shows a unique distribution of photoemission signals relative to the other four controls (Figure 1a−d). The Ni 2p region is dominated by a peak at ∼855.2 eV, missing any contribution from Ni° (at ∼852.9 eV), and the Ni 2p transition associated with NiO near 853.1 eV. Previous XPS/UPS measurements performed on electrochemically oxidized Ni foils have demonstrated a transition between a NiO/$Ni(OH)_2$ layer at less positive oxidizing potentials to a NiO/NiOOH structure at potentials sufficiently positive to evolve oxygen.[89] The observed Ni 2p peak is exclusively shifted to higher binding energies, indicative of Ni^{3+} oxidation states.[69,90] The Auger peak also demonstrates a unique line shape with a shoulder on the high KE/low BE side of the main Auger line, which indicates the presence of unique oxidation states. This is consistent with the formation of γ-NiOOH with some residual hydroxide and is clearly different from the Auger peaks for the oxide films in Figures 1b-d. In the phase diagram by Bode et al, NiOOH has been proposed to exist in two different structures: (i) β-NiOOH with a Ni oxidation state ∼3.0; (ii) γ-NiOOH with a Ni oxidation state ∼3.5−3.7), with different organization and interslab distances.[69,90] The predominant form has been proposed to be γ-NiOOH which is a mixture of Ni^{4+} and Ni^{2+} oxides.[67,90] Electrochemically grown γ-NiOOH typically shows inclusion of alkali ions (from the growth solution) within the crystal lattice,[67] which were confirmed, with easily

Table 2. Binding Energies and Percent Compositions for O 1s Peaks in Figure 2[a]

	O 1s	% composition	Ni $2p_{3/2}$	Ni $2p_{1/2}$	Ni $2p_{1/2-3/2}$	Ni $2p_{intersite}$[i]	Ni $2p_{satellite}$	α	α'
AD-s-NiO_x	529.7[b]	39.9	854.7[h]	872.4[h]	17.7	857.8	861.8	1698.0	1702.8
	531.1[c]	39.1	856.4[k]	874.3[k]	18.0			1699.7	1704.4
	531.8[f]	11.7							
	532.7[d]	9.3							
Ar-s-NiO_x	529.6[b]	66.8	853.1[g]	870.1[g]	17.0	858.0	862.3	1699.0	
	530.9[c]	26.8	854.8[h]	872.6[h]	17.9			1700.7	
	532.0[d]	6.4	856.4[h]	874.7[h]	18.3			1702.3	
OP-s-NiO_x	529.4[b]	40.2	855.3[h]	872.9[h]	17.5	858.4	862.5	1699.6	1703.7
	530.7[c]	31.5	856.9[k]	874.6[k]	17.6			1701.2	1705.3
	531.9[f]	20.0							
	532.9[d]	8.3							

[a]$\alpha' = KE_{Auger} + BE_{photoelectron}$; α'' uses the higher kinetic energy (lower binding energy) shoulder of the Auger peak. [b]O 1s component of NiO. [c]O 1s component of $Ni(OH)_2$. [d]O 1s from physisorbed H_2O. [e]O 1s from Ni_2O_3. [f]O 1s from NiOOH. [g]Metallic Ni character. [h]Ni 2p for NiO/$Ni(OH)_2$. [i]Ni $2p_{3/2\ intersite}$. [j]Ni 2p for Ni_2O_3. [k]Ni 2p for NiOOH.

detectable levels of potassium ions in the XPS data for the sample in Figure 1e.

XPS of Solution-Processed NiO_x Films. Figure 2 shows the O 1s, Ni 2p and LVV Ni Auger spectra for three different s-NiO_x films deposited on gold foils: (i) AD-s-NiO_x, (ii) Ar-s-NiO_x, and (iii) OP-s-NiO_x. Comparable results were obtained with pretreatments of s-NiO_x on ITO and gold substrates; however, gold foils eliminate confusing the O 1s spectra in the NiO_x film with components from indium tin oxide (ITO) substrates. Peaks were fit with the components used in the standards XPS data in Figure 1 and the binding energies and relative atomic percentages for each component are presented in Table 2.

AD-s-NiO_x Film. In Figure 2a, the two most prominent O 1s peaks (529.7 and 531.1 eV) indicate that the majority of the AD-s-NiO_x processed at temperatures below 200 °C is a mixture of NiO and $Ni(OH)_2$.[67] The highest binding energy component in each of the O 1s spectra was judged not to be due to carbon contaminants; the sample-to-sample variations in the contributions of this peak did not correlate with changes in relative C 1s peak area. The Ni 2p spectra and the small, higher binding energy shoulder of the Ni Auger spectra suggest the presence of higher order nickel oxidation states, along with adsorbed water. The higher-order states are attributed to the oxy-hydroxide (NiOOH) component, as Ni_2O_3 is not as stable at low temperatures in the presence of water.

Ar-s-NiO_x Film. Figure 2b shows the XPS data of Ar-s-NiO_x films. Ar ion bombardment causes preferential loss of oxygen, resulting in reduction of the oxide to Ni metal.[72,83,85,91−93] From the O 1s spectrum, it appears as if the predominant O 1s component removed by the sputtering process is associated with surface hydroxyl species, with residual physisorbed water remaining. A low BE shoulder appears in the Ni 2p spectrum at ~853.1 eV for Ni $2p_{3/2}$ and 870.1 eV for Ni $2p_{1/2}$, suggesting the presence of Ni^0, further corroborated by the Ni$2p_{1/2}$ − Ni$2p_{3/2}$ separation of 17.0 eV. There does appear to be three clear components in both the Ni $2p_{3/2}$ and Ni $2p_{1/2}$ spectra, possibly suggesting that Ni^{3+}-like defect states are introduced, arising from charge neutralization within the oxide film. Unlike the standards containing higher-order nickel oxidation states, the α parameters remain consistent with the presence of Ni^{2+} species. Thus, one can conclude the three components are metallic nickel and resolved NiO and $Ni(OH)_2$ in the Ni 2p spectrum. In Figure 2b, NiO and $Ni(OH)_2$ are both grouped under one assignment, representing a single oxidation state of nickel.

OP-s-NiO_x Film. Figure 2c shows the XPS spectra of the OP-s-NiO_x film. O_2-plasma treatment has been deemed essential to achieve the chemical wetting and electronic properties required for hole-selective interlayers in OPVs based on polymer:fullerene BHJs.[50,51] The O_2 plasma treatment appears to dramatically change the O 1s spectrum, with the higher binding energy components becoming more pronounced. There is also a shift in the Ni 2p spectrum toward higher binding energy and a change in the relative intensities of the Ni 2p peaks. Unlike the AD-s-NiOx, there is little ambiguity with comparison to the standards in Figure 1, indicating these peak shapes and distributions are consistent with a mixture of NiO, $Ni(OH)_2$, and NiOOH states. It is hypothesized that the O_2 plasma treatment results in both β- and γ-NiOOH phases, as well as an underlying NiO/$Ni(OH)_2$ layer. This conclusion is further collaborated by the valence structure of the Ni Auger line in Figure 2c and the high binding energy shift of the Ni $2p_{3/2}$ components. The highest binding energy component in the O 1s spectrum is attributed to physisorbed water.

The presence of oxyhydroxide components in these NiO_x films, as well as the demonstrated spectral shapes, differs from what has been previously hypothesized for NiO_x interlayers.[38,39,49,52,53,56,94] Previous reports have suggested that O_2-plasma treatment of NiO films (deposited by sputtering) introduces higher-order oxide components, attributed only to Ni_2O_3, with Ni^{3+} defect states that p-dope the film.[38,56,94] However, the presence of a stoichiometric Ni^{3+} oxide (Ni_2O_3) seems less probable than NiOOH. Ni_2O_3 has a trigonal hexagonal crystal structure similar to Al_2O_3, while both the β-NiOOH and $Ni(OH)_2$ have a rhombohedral structure.[69] It is not anticipated that sufficient energy has been induced by annealing and the O_2-plasma treatment to induce such a crystallographic reorganization. A Ni_2O_3 layer also seems improbable since process temperatures in excess of 250 °C are required for dehydration/dehydroxylation and conversion to the higher order oxide.[55,68,84−87] Only by performing a detailed study with the rigorous standards given in Figure 1 were we able to uniquely identify the presence of the oxy-hydroxide. The presence of NiOOH, a dipole species, and not Ni_2O_3, an artifact of p-doping, will have direct impact on understanding device performance, as discussed below.

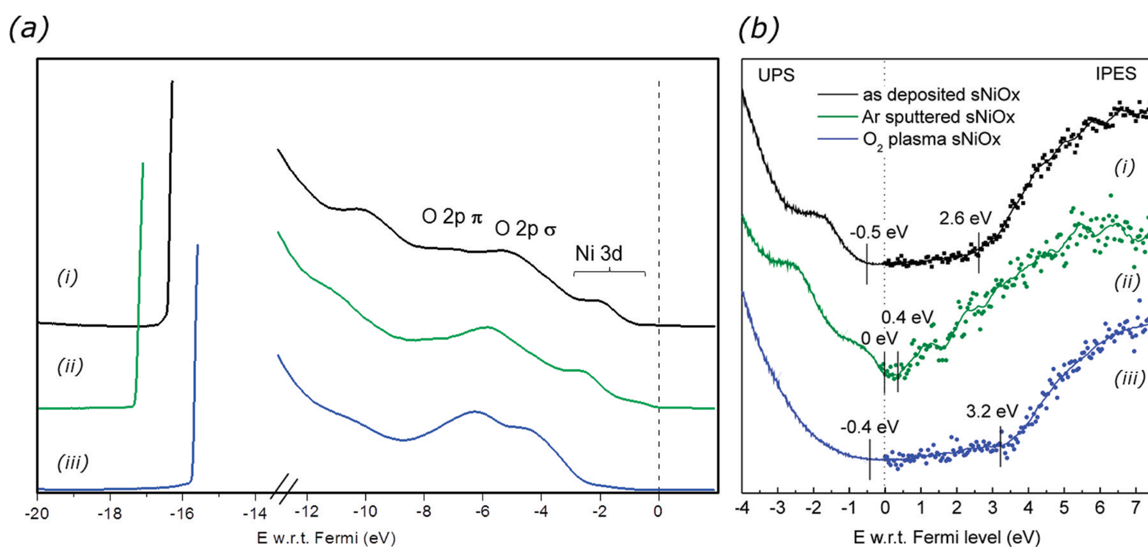

Figure 3. (a) UPS and (b) UPS/IPES of the different pretreated s-NiO_x films (i) as-deposited, (ii) Ar-ion-sputtered, and (iii). O_2 plasma-treated. The UPS and IPES spectra of the different pretreatments of NiO_x films in b were used to define the bandgap stated in Figure 4b. It is important to note that the UPS spectra in a and b show the same valence band and relative Fermi edges, but were taken with different instruments.

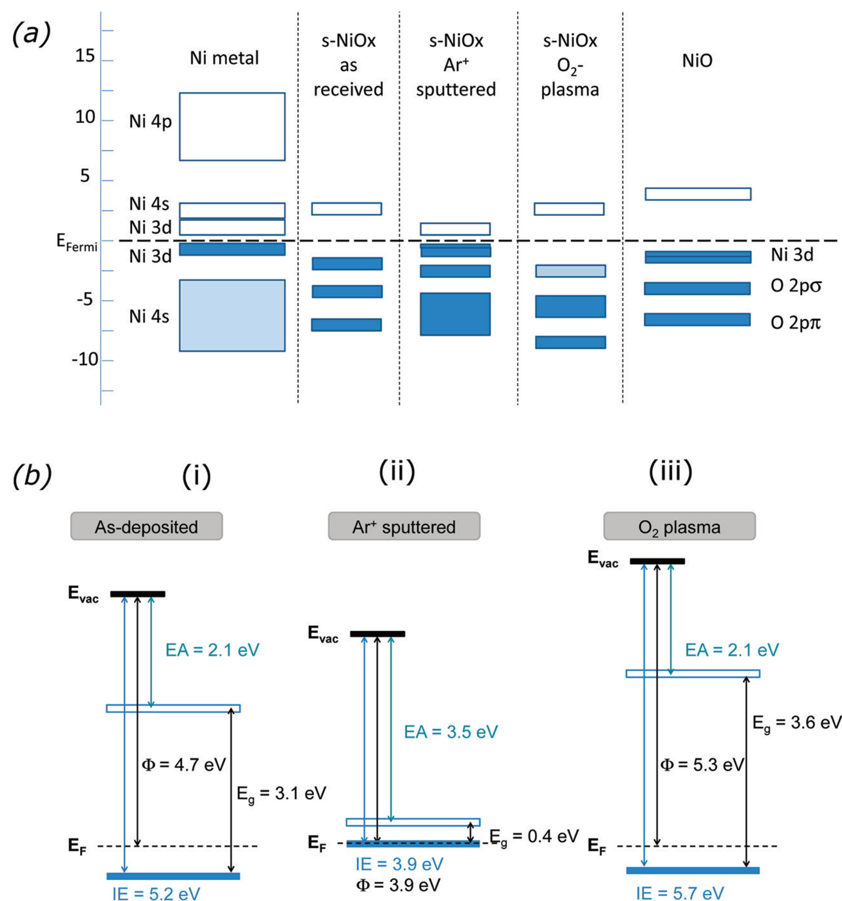

Figure 4. (a) Valence orbital labels and relative energies with respect to the Fermi level for Ni metal and NiO, as discussed in the text and derived from experimental and theoretical evidence. Valence orbital peaks determined in Figure 3 for the different pretreatments are also included for reference. (b) Proposed energy band diagrams for the different pretreatments of s-NiO_xfilms: (i) as-deposited, (ii) Ar ion-sputtered, and (iii) O_2 plasma-treated.

UPS/IPES of s-NiO_x Films. Photoelectron spectroscopy can be a useful tool for probing the work function (Φ), ionization energy (IE), and electron affinity (EA) of a thin, conductive film, using UPS and IPES, respectively. In these techniques, the Φ, IE, and EA are all defined as energy separations from the surface specific vacuum level, and not an infinite vacuum level common to all surfaces.[95−97] Because of this definition, all three key parameters can be susceptible to

surface dipole species such as NiOOH as well as effective p-doping, such as Ni_2O_3. By combining the surface species evaluation discussed above with UPS and IPES, a more clear understanding of the interfacial phenomena affecting the performance of NiO_x interlayers can be achieved.

Figure 3 (i, ii, and iii) shows the UPS and IPES results for as-deposited, Ar ion-sputtered, and O_2-plasma treated s-NiO_x films respectively. Figure 4 summarizes the valence orbital energy levels and how they are altered for various nickel oxides (Figure 4a) and the proposed electrical band edge energies inferred from the UPS/IPES data (Figure 4b). As described in Figure 4a, the valence band for NiO_x is comprised of the occupied Ni 3d and O 2p orbitals while the conduction band is composed of the unoccupied Ni 3d, Ni 4s, and Ni 4p orbitals, with the ground state configuration of $Ni3d^8O2p^6$.[60,98−100] In Figure 3a, curve i, the UPS of the AD-s-NiO_x film shows a feature at ∼2 eV below the Fermi level attributed to localized Ni 3d states, and an O 2p band from approximately −4 to −7 eV, with a subtle splitting feature. The splitting of the O 2p orbitals arises from the differentiated five Ni 3d levels, which are split into a triply degenerate t_{2g} level and a doubly degenerate e_g level,[83] consistent with the different symmetries associated with the Ni $3d_{xy}$, $3d_{xy}$, and $3d_{yz}$ for the t_{2g} orbitals and the Ni $3d_{x2-y2}$ and $3d_{z2}$ for the e_g orbitals, as illustrated in Figure 4a. This results in different interactions with the O 2p orbital, causing splitting of the O 2p band into the O $2p_\pi$ (∼7 eV) and O $2p_\sigma$ (∼4.8 eV) bands.[83,101] The molecular diagram shows further splitting of the t_{2g} and e_g bands, according to spin up and down, resulting in the t_{2g} (↑), t_{2g} (↓), and e_g(↑) comprising the occupied orbitals and the e_g (↓) as the unoccupied orbital.[102] The IPES data for the AD-s-NiO_x (Figure 3b, curve i) exhibits a broad feature at ∼2.6 eV above the Fermi level, indicating the onset of the conduction band comprised of empty Ni 3d states. For NiO, the conduction band is proposed to be composed from the $Ni3d^9O2p^6$ state at ∼4 eV above the Fermi level, with the final state found to be the $Ni3d^{10}O2p^5$ calculated to be 14 eV above the first band. [83,102] From the combination of IPES and UPS data, the energetic band gap is estimated at ∼3.1 eV, with a Φ ∼4.7 eV, an IE ∼5.2 eV and an EA ∼ 2.1 eV for AD-s-NiO_x, as summarized in Figure 4, panel i.

The UPS/IPES of the Ar-s-NiOx films shown in Figure 3, panel ii, present unique valence and conduction band structure to the AD-s-NiO_x films. Previous reports of Ar ion sputtering have demonstrated preferential removal of the O^{2-} ions by the Ar ion bombardment, as consistent with the XPS results in Figure 2b.[83,103] There is clear indication of metallic nickel-like ground state, with a ground state configuration of $3d^94sp^1$. It is generally accepted that there is a definite hybridization of orbitals for the unoccupied states over the occupied states[104] and the Ni 3d valence states have been suggested to be of ∼90% 3d character,[105] although there are also calculations that suggest a certain degree of hybridization among the 3d, 4s, and 4p valence orbitals.[106] In the UPS of the Ar-s-NiOx film Figure 3 ii, the metallic like character is demonstrated with the exposure of the Ni 3d feature within ∼0.5 eV of the Fermi level and an additional Ni 3d feature at ∼1.5 eV below the Fermi level, which is associated with the majority and minority spins of a nearly localized Ni 3d band.[83,106,107] There is also a lower intensity feature from the Ni 4s structure at ∼3 to 9 eV below the Fermi for metallic Ni, as suggested by the molecular diagram in Figure 4a.[108] The unfilled states, as measured by IPES, are comprised of unoccupied Ni 3d states just above the Fermi level[109−112] as well as empty Ni 4s states at ∼1.1 to 1.4 eV above the Fermi level.[113] Attribution to the Ni 4p band is at approximately 7 eV above the Fermi level.[111] However, the O 2p features, as seen in the AD-s-NiOx spectrum persist, indicating that full conversion to metallic Ni has not taken place, also consistent with the XPS results discussed above. This O 2p-like feature in the region 4−10 eV below the Fermi level may also arise from Ni 4s character emerging ∼3 eV below the Fermi level, causing some additional broadening of this photoemission peak. The IPES data in Figure 3b, plot ii, suggests an electronic structure consistent with the emergence of the Ni 3d/Ni 4s structure of metallic Ni, yielding a decrease in both Φ and IE of ∼3.9 eV, with an EA at ∼3.5 eV and an electronic band gap of ∼0.4 eV, as summarized in Figure 4b, panel ii.

OP-s-NiO_x shows a predominant decrease in the Ni 3d feature at ∼2 eV below the Fermi level Figure 3a, plot iii, although there is still residual evidence of the Ni 3d emission feature (Figure 4b). There is a more pronounced O2p peak separation into σ and π components, demonstrated by the features at ∼4 eV and ∼6 eV below the Fermi level, respectively.[83,101] These features have been shifted to lower energies with respect to the Fermi edge (toward higher binding energies) versus AD-s-NiO_x. The IPES data (Figure 3b, plot iii) shows the unfilled Ni 3d state, similar to that of the as-deposited s-NiO_x, but at a higher energy with respect to the Fermi level (∼3.2 versus 2.6 eV), yielding a striking increase in the electronic bandgap energy to 3.6 eV, which is significant for the use of this material as an OPV interlayer. Overall, the surface exhibits an increase in Φ to ∼5.3 eV and the IE to ∼5.7 eV (Figure 4b). The UPS/IPES data for the OP-s-NiO_x further confirms the XPS results discussed above: the O_2-plasma etch does not appear to extensively p-dope the oxide. If the oxide was sufficiently p-doped, the enthalpy of formation for midgap states would also be affected; evidence for these states within the charge transfer gap of p-doped NiO with Li^+ has been previously reported with the detection of a peak at ∼1.2 eV above the Fermi level in IPES.[60] The significant change in the vacuum level shift between the AD-s-NiO_x and OP-s-NiO_x films, (ΔE_{vac} ≈ +0.5 eV) as seen from the shift of the photoemission cutoff in Figure 3 i and iii, result in a significant increase in both the Φ and IE of the film post O_2 plasma treatment (Figure 4b). This large vacuum level shift implies the formation of a strong dipole upon plasma treatment, again consistent with an oxyhydroxide species and not necessarily Ni_2O_3. A recent theoretical calculation by Van der Ven et al.[114] hypothesizes a transition in the crystal structure from the established T1 oxygen stacking (ABAB) for $Ni(OH)_2$[115,116] to a theoretical P3 oxygen stacking (AABBCC). The result is a surface of O−Ni−OH, creating a unique surface dipole from a predominantly hydroxylated surface, consistent with the differences in the UPS measurements for the AD-s-NiO_x and OP-s-NiO_x. The observed changes in the band edge energetics for OP-s-NiO_x films, which are dictated by near-surface composition changes, are critical to the performance of these interlayers in OPVs, as discussed further below.

Figure 5 gives the optical absorbance spectrum for the AD- and OP-s-NiOx films. The onset of absorption provides an estimate of the optical band gaps, which is 3.8 (±0.2) eV for the as-deposited s-NiO_x film and ∼3.6 (±0.2) eV for the O_2-plasma-treated s-NiO_x film. These are changes in the bulk band gap energy for s-NiO_x and are quite different from the band gap energies inferred from the UPS/IPES data. The changes in Φ

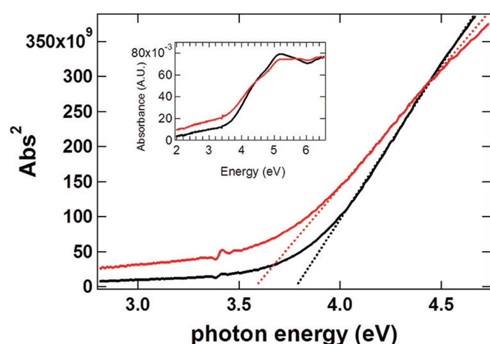

Figure 5. Optical absorbance spectra (solid lines) and optical band gap fits for AD-s-NiO_x (black lines) and OP-s-NiO_x (red lines) films on quartz. The inset shows the raw absorbance data. The optical gap decreases from ∼3.8 (±0.2) eV for the as-deposited film to ∼3.6 (±0.2) eV post-O_2 plasma treatment.

and IE measured using UPS/IPES spectroscopy are extremely surface sensitive and are attributed to a combination of a vacuum level shift due to the presence of NiOOH on the surface and a slight increase in p-doping of the oxide film. The contribution of p-doping of the oxide is hypothesized to be a much less significant effect. The optical gap differences with pretreatment are statistically similar, whereas the electronic gaps discussed above are quite different. We therefore conclude again that the electronic measurements are surface sensitive and not representative of the bulk band gap.

***J−V* Behavior of As-Deposited versus O_2-Plasma-Treated s-NiO_x Interlayers.** Previous studies on the device implications of NiO_x interlayers have anticipated that changes in near-surface composition and band edge energies for s-NiO_x films would impact on hole-selectivity in charge harvesting through these interlayer films (via electron blocking).[50,51,54,57] The AD- and OP-s-NiOx interlayers are compared using the current density−voltage (*J*−*V*) behavior in diode-like device platforms designed to test the rectification and electron-blocking capabilities of the NiO_x interlayers, exploring both $PC_{61}BM/NiO_x$ and P3HT:$PC_{61}BM/NiO_x$ heterojunctions.

Figure 6 demonstrates the *J*−*V* rectification of device platforms (ITO/NiO_x/$PC_{61}BM$/Ca:Al) designed to test the electron-blocking, hole-selective capabilities of the AD- and OP-s-NiO_x interlayers. The linear and log form of the *J*−*V* curves are plotted in Figures 6a and 6b, respectively. The energy diagrams in Figures 6c and 6d were estimated from UPS measurements of $PC_{61}BM$ on differently treated oxide interlayers. The LUMO of $PC_{61}BM$ was estimated from previously reported IPES measurements.[117] Given the energy diagrams for these materials, *J*−*V* behavior is expected to be analogous to planar, type II heterojunctions in the dark.

Both heterojunctions are rectifying; at forward bias, hole-injection into the NiO_x interlayer and electron-injection into the fullerene layer leads to recombination limited currents, with

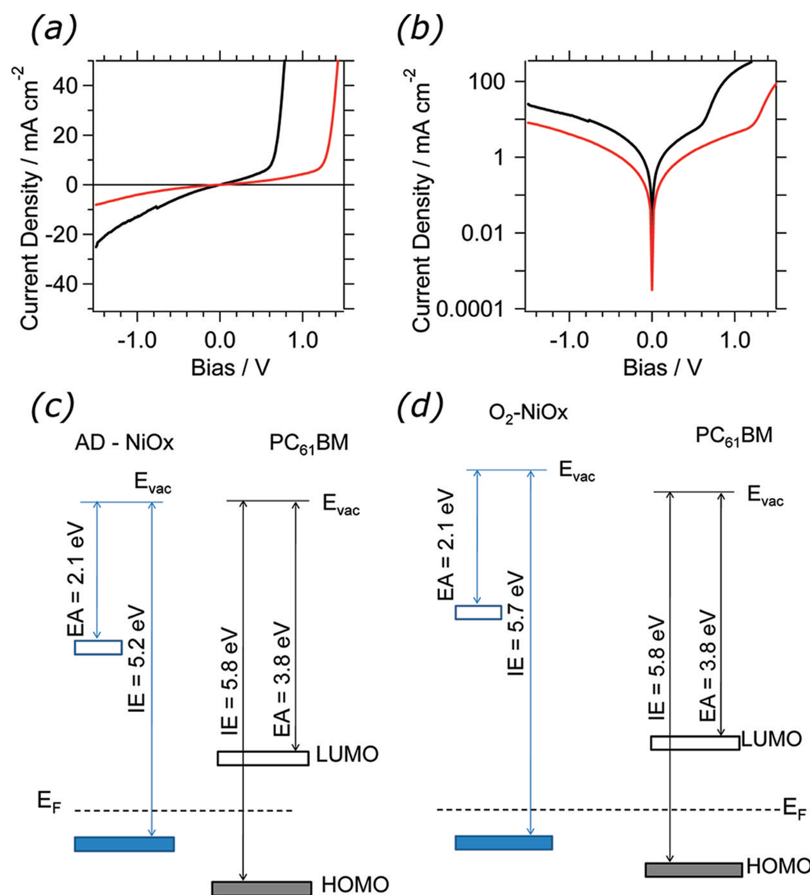

Figure 6. (a) Linear and (b) log plots of *J*−*V* characteristics of electron-only devices for as-deposited (black lines) and O_2-plasma-treated (redl ines) s-NiOx interlayer devices. Structure is ITO/s-NiOx/$PC_{61}BM$/Ca/Al. (c) Proposed energy diagrams for the as-deposited and (d) O_2-plasma-treated s-NiOx interlayer with the fullerene.

a significantly higher forward bias onset voltage for the OP-s-NiO_x films. This increased onset voltage is consistent with the change observed in the energy gap ($E_{VB,\ NiOx} - E_{LUMO,\ PCBM}$) upon O_2-plasma treatment (Figure 4b). Near zero bias and at reverse bias, the diode-based on the OP-s-NiO_x film demonstrates a significantly reduced reverse saturation current (ca. 100x lower at zero bias), with higher voltages obtained prior to breakdown. This current is the result of: (i) overcoming the energetic barrier between the interlayer and the ITO, which is quite large; or (ii) leakage pathways between the ITO Fermi level and the NiO_x gap states or through pinholes, analogous to leakage current in a type II heterojunction. However, there is no barrier for electrons from the conduction band of the NiO_x into the fullerene. The leakage current between via pinholes and the midgap states of the NiO_x and the ITO seems most probable. At sufficient field strength even the OP-s-NiO_x film allows for electron injection; however, such field strengths are unlikely to be obtained in working OPVs. The J-V curves for the electron-only devices further confirm the photoelectron spectroscopy results above, indicating minimal p-doping of the oxide. If the O_2 plasma treatment was acting only to p-dope the material (as in previously ascribed cases of Ni_2O_3),[38,39,49,52,53,56,94] a higher degree of leakage current, due an increase of midgap states, is expected over the AD-s-NiO_x interlayer. However, if the predominant surface affect upon O_2 plasma etch is to introduce an interface dipole, which alters the band edge energies and local vacuum level (NiOOH), the amount of leakage current should be reduced. The combined conclusions from the XPS, UPS, IPES, and optical data all indicate that the enhanced electron blocking properties of the OP-s-NiO_x films are attributed to the formation of the surface dipole, which prevents electrons from being collected at the oxide/fullerene interface, relative to the AD-NiOx layer. Thus, proper control and manipulation of the local interfacial dipole appears to be sufficient for improved electron-blocking properties of the oxide film.

The ability to more efficiently block electrons at the interlayer is demonstrated in full P3HT:PC_{61}BM BHJ OPVs, as shown in Figure 7, with device parameters presented in Table 3 and expanded linear and log J-V curves given in the Supporting Information section. The AD-s-NiO_x interlayer produces an OPV response with an open circuit voltage (V_{OC}) of 0.49 V, a short-circuit photocurrent (J_{SC}) of 10.1 mA/cm^2, and a fill factor of 0.54, resulting in an overall efficiency of 2.7%. The OP-s-NiOx interlayer increases the V_{OC} to 0.58 V and results in an insignificant decrease in J_{SC} (9.7 mA/cm^2). However, the fill factor of the O_2-plasma treated interlayer devices was significantly higher (0.67), yielding an overall efficiency increase to 3.7%. The increase in the V_{OC} can be explained through a decrease in the density of states at the valence band edge of the NiO_x interlayer. By eliminating the Ni 3d states from the valence band upon O_2-plasma treatment, midgap states are reduced and/or are not accessible due to the presence of the dipole at the surface. The leakage current and recombination at the interface are both decreased, resulting in an increase in V_{OC}. The improvement is attributable to a significant decrease in recombination probabilities, derived from the improved electron-blocking properties of the OP-s-NiO_x interlayer.

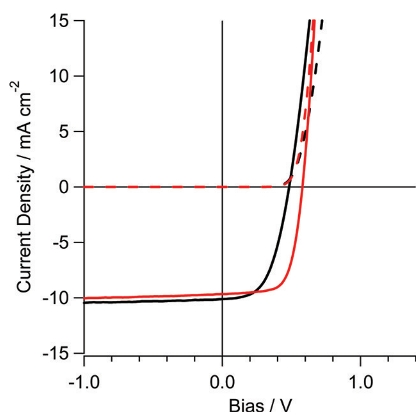

Figure 7. $J-V$ characteristics for typical (black lines) AD-NiOx and (red lines) O_2-plasma-treated NiOx interlayer devices constructed with P3HT:PC_{61}BM BHJs. Device parameters are provided in Table 3 and full linear and semilog plots are provided in the Supporting Information.

Table 3. Device Parameters for Figure 7

	AD-s-NiO_x	OP-s-NiO_x
V_{oc} (V)	0.49 (±0.03)	0.58 (±0.01)
J_{sc} (mA cm^{-2})	−10.1 (± 0.1)	−9.7 (± 0.2)
FF	0.54 (± 0.01)	0.67 (± 0.01)
eff.	2.7 (± 0.1)	3.7 (± 0.1)
J_0 (mA cm^{-2})	6.6 (± 1.7) × 10^{-7}	1.6 (± 3.2) × 10^{-7}
$R_{series,dark}$ (Ω cm^{-2})	5.9 (± 1.0)	2.6 (0.2)
$R_{shunt,dark}$ (Ω cm^{-2})	5.2 (± 7.6) × 10^5	2.5 (± 1.6) × 10^5
$R_{series,light}$ (Ω cm^{-2})	5.2 (± 0.5)	2.6 (± 0.2)
$R_{shunt,light}$ (Ω cm^{-2})	4.1 (± 1.4) × 10^3	4.0 (± 1.7) × 10^3
degree of rectification[a] dark	42 000 (± 49 000)	57 000 (± 45 000)
degree of rectification[a] light	6.9 (± 0.6)	11.3 (± 0.8)

[a]degree of rectification is determined by comparing the current densities at ±1 V in the OPV.

If one assumes that the relative Fermi level for holes ($E_{F,holes}$) is pinned in both cases to the Fermi level of the interlayer (4.7 eV versus 5.3 eV for O_2 plasma)[118−121] and the relative Fermi level for electrons ($E_{F,electrons}$) is dictated by top contact and thus unchanged, an increase in the V_{OC} of the device is also predicted for the O_2-plasma treated device by creating a larger $E_{F,electrons} - E_{F,holes}$ offset. However, pinning the $E_{F,holes}$ at a deeper level, relative to vacuum, may also decrease the HOMO−HOMO offset for the P3HT and PC_{61}BM and a decrease in charge generation within the blend is expected (possibly decreasing the short circuit current of the device).[7,57,121] However, no evidence for changes in charge carriers was detected. Energy level alignment studies are part of current and future research to study and understand the interface of the NiO_x with different active layers.

■ CONCLUSIONS

Solution-processed NiO_x represents one of several oxide interlayers currently being explored for OPV applications, with emphasis on selectivity for the collection of holes while having a high bandgap to block electrons from acceptors. The treatment of the films with an O_2-plasma provides a significant increase in the work function (from 4.7 to 5.3 eV) and is largely attributed to an increase in concentration of NiOOH species on the surface, resulting in a large surface dipole. The plasma treatment shows a reduction in the near-Fermi edge density of

Ni 3d states of the valence, but has little impact on the conduction band. The measured change in the valence structure, combined with the surface dipole, serve to enhance the electron blocking characteristics from both the fullerene $PC_{61}BM$ and the leakage current from the ITO into the midgap states of the NiO_x. The result is an increase in V_{OC}, attributed to the reduction in both the leakage current and recombination at the NiO_x/BHJ interface. It may be possible that the surface chemistries are locally controlling the energetics of the subsequent blend layer or inducing unique ordering of the blend directly on the oxide. Regardless, the presence and increased concentration of NiOOH species following O_2 plasma treatment indicate that the oxide/organic interface is particularly important when these interlayers are included in OPVs. The high level of interfacial forces present at the surface signifies that these interfaces are sufficiently more complex than the assumed van der Walls controlled interfaces of organic/organic layers (namely PEDOT:PSS and subsequent blends).[118,120,121] Understanding the nature of interactions, the effect of ionic versus covalently bound interlayers on the interface, and how these interlayers improve device performance continue to be a point of debate and interest and will be the focus of future works.

■ ASSOCIATED CONTENT

Ⓢ Supporting Information

Theoretical summary of electrical band gap, experimental procedures, expanded Auger peaks for pretreatments of s-NiO_x films, and linear and log current density−voltage plots for full bulk heterojunction devices. This material is available free of charge via the Internet http://pubs.acs.org.

■ AUTHOR INFORMATION

Corresponding Author

*E-mail" ratcliff@email.arizona.edu (E.L.R.); nra@email.arizona.edu (N.R.A.).

■ ACKNOWLEDGMENTS

Research supported as part of the Center for Interface Science: Solar Electric Materials, an Energy Frontier Research Center funded the U.S. Department of Energy, Office of Science, Office of Basic Energy Sciences, under Award Number DE-SC0001084 (NRA, JJB, AG, DSG, ELR), as part of the Center for Energy Efficient Materials, an Energy Frontier Research Center funded the U.S. Department of Energy, Office of Science, Office of Basic Energy Sciences, under Award Number DE-SC0001009 (DCO, KXS), NSF DMR-1005892 (AK), and the Deutsche Forschungsgemeinschaft (DFG) postdoctoral fellowship program (JM).

■ REFERENCES

(1) Park, S. H.; Roy, A.; Beaupre, S.; Cho, S.; Coates, N.; Moon, J. S.; Moses, D.; Leclerc, M.; Lee, K.; Heeger, A. J. *Nat. Photonics* **2009**, *3* (5), 297−U5.

(2) Brabec, C. J. D. J. R. *MRS Bull.* **2008**, *33*, 670−675.

(3) Chen, H. Y.; Hou, J. H.; Zhang, S. Q.; Liang, Y. Y.; Yang, G. W.; Yang, Y.; Yu, L. P.; Wu, Y.; Li, G. *Nat. Photonics* **2009**, *3* (11), 649−653.

(4) Venkataraman, D.; Yurt, S.; Venkatraman, B. H.; Gavvalapalli, N. *J. Phys. Chem. Lett.* **2010**, *1* (6), 947−958.

(5) Wynands, D.; Mannig, B.; Riede, M.; Leo, K.; Brier, E.; Reinold, E.; Bauerle, P. *J. Appl. Phys.* **2009**, *106* (5), 5.

(6) Yi, Y. P.; Coropceanu, V.; Bredas, J. L. *J. Am. Chem. Soc.* **2009**, *131* (43), 15777−15783.

(7) Ratcliff, E. L.; Zacher, B.; Armstrong, N. R. *J. Phys. Chem. Lett.* **2011**, *2* (11), 1337−1350.

(8) Steim, R.; Kogler, F. R.; Brabec, C. J. *J. Mater. Chem.* **2010**, *20* (13), 2499−2512.

(9) Hains, A. W.; Liu, J.; Martinson, A. B. F.; Irwin, M. D.; Marks, T. J. *Adv. Funct. Mater.* **2010**, *20* (4), 595−606.

(10) Wagenpfahl, A.; Deibel, C.; Dyakonov, V. *IEEE J. Sel. Top. Quantum Electron.* **2010**, *16* (6), 1759−1763.

(11) Wagenpfahl, A.; Rauh, D.; Binder, M.; Deibel, C.; Dyakonov, V. *Phys. Rev. B* **2010**, *82* (11), No. 115306.

(12) Zhang, Y.; Dang, X.-D.; Kim, C.; Nguyen, T.-Q. *Adv. Energy Mater.* **2011**, *1* (4), 610−617.

(13) Arkhipov, V. I.; Heremans, P.; Bassler, H. *Appl. Phys. Lett.* **2003**, *82* (25), 4605−4607.

(14) Koster, L. J. A.; Mihailetchi, V. D.; Blom, P. W. M. *Appl. Phys. Lett.* **2006**, *88* (9), 093511−093514.

(15) Koster, L. J. A.; Mihailetchi, V. D.; Blom, P. W. M. *Appl. Phys. Lett.* **2006**, *88* (5), 052104−052107.

(16) Langevin, P. *Ann. Chim. Phys.* **1903**, *28*, 433−530.

(17) Liu, A.; Zhao, S.; Rim, S. B.; Wu, J.; Konemann, M.; Erk, P.; Peumans, P. *Adv. Mater.* **2008**, *20* (5), 1065−+.

(18) Mandoc, M. M.; Koster, L. J. A.; Blom, P. W. M. *Appl. Phys. Lett.* **2007**, *90* (13), No. 133504.

(19) Nunzi, J. M.; Juska, G.; Jean, F.; Arlauskas, K. *Acta Phys. Pol., A* **2005**, *107* (2), 377−380.

(20) Peumans, P.; Yakimov, A.; Forrest, S. R. *J. Appl. Phys.* **2003**, *93* (7), 3693−3723.

(21) Pivrikas, A.; Juska, G.; Mozer, A. J.; Scharber, M.; Arlauskas, K.; Sariciftci, N. S.; Stubb, H.; Osterbacka, R. *Phys. Rev. Lett.* **2005**, *94* (17), No. 176806.

(22) Pivrikas, A.; Sariciftci, N. S.; Juska, G.; Osterbacka, R. *Prog. Photovolt.* **2007**, *15* (8), 677−696.

(23) Shuttle, C. G.; Hamilton, R.; O'Regan, B. C.; Nelson, J.; Durrant, J. R. *Proc. Natl. Acad. Sci. U.S.A.* **2010**, *107* (38), 16448−16452.

(24) Shuttle, C. G.; O'Regan, B.; Ballantyne, A. M.; Nelson, J.; Bradley, D. D. C.; Durrant, J. R. *Phys. Rev. B* **2008**, *78* (11), No. 113201.

(25) Cahen, D.; Hodes, G.; Gratzel, M.; Guillemoles, J. F.; Riess, I. *J. Phys. Chem. B* **2000**, *104* (9), 2053−2059.

(26) Potscavage, W. J.; Sharma, A.; Kippelen, B. *Acc. Chem. Res.* **2009**, *42* (11), 1758−1767.

(27) Riede, M.; Mueller, T.; Tress, W.; Schueppel, R.; Leo, K. *Nanotechnology* **2008**, *19* (42), 12.

(28) Wurfel, P. *Chimia* **2007**, *61* (12), 770−774.

(29) Wurfel, P., *Physics of Solar Cells*; Wiley-VCH: Weinheim, Germany, 2005.

(30) Maennig, B.; Drechsel, J.; Gebeyehu, D.; Simon, P.; Kozlowski, F.; Werner, A.; Li, F.; Grundmann, S.; Sonntag, S.; Koch, M.; Leo, K.; Pfeiffer, M.; Hoppe, H.; Meissner, D.; Sariciftci, N. S.; Riedel, I.; Dyakonov, V.; Parisi, J. *Appl. Phys. A* **2004**, *79* (1), 1−14.

(31) Armstrong, N. R.; Veneman, P. A.; Ratcliff, E.; Placencia, D.; Brumbach, M. *Acc. Chem. Res.* **2009**, *42* (11), 1748−1757.

(32) Friedel, B.; Keivanidis, P. E.; Brenner, T. J. K.; Abrusci, A.; McNeill, C. R.; Friend, R. H.; Greenham, N. C. *Macromolecules* **2009**, *42* (17), 6741−6747.

(33) Peisert, H.; Knupfer, M.; Zhang, F.; Petr, A.; Dunsch, L.; Fink, J. *Surf. Sci.* **2004**, *566*, 554−559.

(34) Pingree, L. S. C.; MacLeod, B. A.; Ginger, D. S. *J. Phys. Chem. C* **2008**, *112* (21), 7922−7927.

(35) Ratcliff, E. L.; Jenkins, J. L.; Nebesny, K.; Armstrong, N. R. *Chem. Mater.* **2008**, *20* (18), 5796−5806.

(36) Blom, P. W. M.; Mihailetchi, V. D.; Koster, L. J. A.; Markov, D. E. *Adv. Mater.* **2007**, *19* (12), 1551−1566.

(37) Brenner, T. J. K.; Hwang, I.; Greenham, N. C.; McNeill, C. R. *J. Appl. Phys.* **2010**, *107* (11), No. 114501.

(38) Irwin, M. D.; Buchholz, B.; Hains, A. W.; Chang, R. P. H.; Marks, T. J. *Proc. Natl. Acad. Sci. U.S.A.* **2008**, *105* (8), 2783−2787.
(39) Irwin, M. D.; Servaites, J. D.; Buchholz, D. B.; Leever, B. J.; Liu, J.; Emery, J. D.; Zhang, M.; Song, J.-H.; Durstock, M. F.; Freeman, A. J.; Bedzyk, M. J.; Hersam, M. C.; Chang, R. P. H.; Ratner, M. A.; Marks, T. J. *Chem. Mater.* **2011**, *23* (8), 2218−2226.
(40) Kuwabara, T.; Kawahara, Y.; Yamaguchi, T.; Takahashi, K. *ACS Appl. Mater. Interfaces* **2009**, *1* (10), 2107−2110.
(41) Monson, T. C.; Lloyd, M. T.; Olson, D. C.; Lee, Y. J.; Hsu, J. W. P. *Adv. Mater.* **2008**, *20* (24), 4755−+.
(42) Kroger, M.; Hamwi, S.; Meyer, J.; Riedl, T.; Kowalsky, W.; Kahn, A. *Appl. Phys. Lett.* **2009**, *95* (12), 3.
(43) Meyer, J.; Shu, A.; Kroger, M.; Kahn, A. *Appl. Phys. Lett.* **2010**, *96* (13), 3.
(44) Chan, I. M.; Hong, F. C. *Thin Solid Films* **2004**, *450* (2), 304−311.
(45) Chan, I. M.; Hsu, T. Y.; Hong, F. C. *Appl. Phys. Lett.* **2002**, *81* (10), 1899−1901.
(46) Caruge, J. M.; Halpert, J. E.; Bulovic, V.; Bawendi, M. G. *Nano Lett.* **2006**, *6* (12), 2991−2994.
(47) Wood, V.; Panzer, M. J.; Caruge, J. M.; Halpert, J. E.; Bawendi, M. G.; Bulovic, V. *Nano Lett.* **2010**, *10* (1), 24−29.
(48) Wood, V.; Panzer, M. J.; Halpert, J. E.; Caruge, J. M.; Bawendi, M. G.; Bulovic, V. *ACS Nano* **2009**, *3* (11), 3581−3586.
(49) Betancur, R.; Maymó, M.; Elias, X.; Vuong, L. T.; Martorell, J. *Sol. Energy Mater. Sol. Cells* **2011**, *95* (2), 735−739.
(50) Steirer, K. X.; Chesin, J. P.; Widjonarko, N. E.; Berry, J. J.; Miedaner, A.; Ginley, D. S.; Olson, D. C. *Org. Electron* **2010**, *11* (8), 1414−1418.
(51) Steirer, K. X.; Widjonarko, N. E.; Sigdel, A. K.; Lloyd, M. T.; Ginley, D. S.; Olson, D. C.; Berry, J. J. Optimization of organic photovoltaic devices using tuned mixed metal oxide contact layers. In *35th IEEE Photovoltaic Specialists Conference*; Honolulu, HI, June 20−25, 2010 ; IEEE: Piscataway, NJ, 2010; pp 000102−000104.
(52) Sun, N.; Fang, G.; Qin, P.; Zheng, Q.; Wang, M.; Fan, X.; Cheng, F.; Wan, J.; Zhao, X. *Sol. Energy Mater. Sol. Cells* **2010**, *94* (12), 2328−2331.
(53) Sun, N. H.; Fang, G. J.; Qin, P. L.; Zheng, Q. A.; Wang, M. J.; Fan, X.; Cheng, F.; Wan, J. W.; Zhao, X. Z.; Liu, J. W.; Carroll, D. L.; Ye, J. M. *J. Phys. D: Appl. Phys.s* **2010**, *43* (44), No. 445101.
(54) Berry, J. J.; Widjonarko, N. E.; Bailey, B. A.; Sigdel, A. K.; Ginley, D. S.; Olson, D. C. *IEEE J. Sel. Top. Quantum Electron.* **2010**, *16* (6), 1649−1655.
(55) Norton, P. R.; Tapping, R. L.; Goodale, J. W. *Surf. Sci.* **1977**, *65* (1), 13−36.
(56) Wang, Z. Y.; Lee, S. H.; Kim, D. H.; Kim, J. H.; Park, J. G. *Sol. Energy Mater. Sol. Cells* **2010**, *94* (10), 1591−1596.
(57) Steirer, K. X.; Ndione, P. F.; Edwin Widjonarko, N.; Lloyd, M. T.; Meyer, J.; Ratcliff, E. L.; Kahn, A.; Armstrong, N. R.; Curtis, C. J.; Ginley, D. S.; Berry, J. J.; Olson, D. C. *Adv. Energy Mater.* **2011**, *1* (5), 813−820.
(58) Pourbaix, M. *Atlas of Electrochemical Equilibria in Aqueous Solutions*; Pergamon Press: Oxford, U.K., 1966.
(59) Langell, M. A.; Nassir, M. H. *J. Phys. Chem.* **1995**, *99* (12), 4162−4169.
(60) Reinert, F.; Steiner, P.; Hufner, S.; Schmitt, H.; Fink, J.; Knupfer, M.; Sandl, P.; Bertel, E. *Z. Phys. B: Condens. Matter Quanta* **1995**, *97* (1), 83−93.
(61) Austin, I. G.; Mott, N. F. *Adv. Phys.* **1969**, *18* (71), 41−&.
(62) Bosman, A. J.; Vandaal, H. J. *Adv. Phys.* **1970**, *19* (77), 1−&.
(63) Hufner, S.; Steiner, P.; Reinert, F.; Schmitt, H.; Sandl, P. *Z. Phys. B: Condens. Matter Quanta* **1992**, *88* (2), 247−248.
(64) Kuiper, P.; Kruizinga, G.; Ghijsen, J.; Sawatzky, G. A.; Verweij, H. *Phys. Rev. Lett.* **1989**, *62* (2), 221−224.
(65) Vanelp, J.; Eskes, H.; Kuiper, P.; Sawatzky, G. A. *Phys Rev. B* **1992**, *45* (4), 1612−1622.
(66) Adler, D.; Feinleib, J. *Phys. Rev. B* **1970**, *2* (8), 3112−3134.
(67) Beverskog, B.; Puigdomenech, I. *Corros. Sci.* **1997**, *39* (5), 969−980.
(68) Scheidt, H.; Globl, M.; Dose, V. *Surf. Sci.* **1981**, *112* (1−2), 97−110.
(69) Bode, H.; Dehmelt, K.; Witte, J. *Electrochim. Acta* **1966**, *11* (8), 1079−1087.
(70) Juodkazis, K.; Juodkazyte, J.; Vilkauskaite, R.; Jasulaitiene, V. *J. Solid-State Electrochem.* **2008**, *12* (11), 1469−1479.
(71) Biesinger, M. C.; Payne, B. P.; Grosvenor, A. P.; Lau, L. W. M.; Gerson, A. R.; Smart, R. S. *Appl. Surf. Sci.* **2011**, *257* (7), 2717−2730.
(72) Oswald, S.; Bruckner, W. *Surf. Interface Anal.* **2004**, *36* (1), 17−22.
(73) Gaskell, K. J.; Starace, A.; Langell, M. A. *J. Phys. Chem. C* **2007**, *111* (37), 13912−13921.
(74) Atanasov, M.; Reinen, D. *J. Electron Spectrosc. Relat. Phenom.* **1997**, *86* (1−3), 185−199.
(75) Uhlenbrock, S.; Scharfschwerdt, C.; Neumann, M.; Illing, G.; Freund, H. J. *J. Phys.: Condens. Matter* **1992**, *4* (40), 7973−7978.
(76) Vanveenendaal, M. A.; Sawatzky, G. A. *Phys. Rev. Lett.* **1993**, *70* (16), 2459−2462.
(77) Grosvenor, A. P.; Biesinger, M. C.; Smart, R. S.; McIntyre, N. S. *Surf. Sci.* **2006**, *600* (9), 1771−1779.
(78) Biesinger, M. C.; Payne, B. P.; Lau, L. W. M.; Gerson, A.; Smart, R. S. C. *Surf. Interface Anal.* **2009**, *41* (4), 324−332.
(79) Gupta, R. P.; Sen, S. K. *Phys. Rev. B* **1974**, *10* (1), 71−77.
(80) Gupta, R. P.; Sen, S. K. *Phys. Rev. B* **1975**, *12* (1), 15−19.
(81) Briggs, D.; Seah, M. P., *Practical Surface Analysis: By Auger and X-Ray Photoelectron Spectroscopy*; Wiley: New York, 1983.
(82) Wagner, C. D.; Muilenberg, G. E., *Handbook of X-ray Photoelectron Spectroscopy: A Reference Book of Standard Data for Use in X-ray Photoelectron Spectroscopy*; Physical Electronics Division, Perkin-Elmer Corp.: Eden Prairie, MN, 1979.
(83) Hagelin-Weaver, H. A. E.; Weaver, J. F.; Hoflund, G. B.; Salaita, G. N. *J. Electron Spectrosc. Relat. Phenom.* **2004**, *134* (2−3), 139−171.
(84) Evans, S.; Pielaszek, J.; Thomas, J. M. *Surf. Sci.* **1976**, *55* (2), 644−662.
(85) Kim, K. S.; Winograd, N. *Surf. Sci.* **1974**, *43* (2), 625−643.
(86) Krishnan, N. G.; Delgass, W. N.; Robertson, W. D. *Surf. Sci.* **1976**, *57* (1), 1−11.
(87) Wagner, N.; Brummer, O.; Khodasevich, V. V. *Phys. Status Solidi A* **1980**, *62* (1), 275−282.
(88) Bockris, J. O.; Otagawa, T. *J. Electrochem. Soc.* **1984**, *131* (2), 290−302.
(89) Hoppe, H. W.; Strehblow, H. H. *Surf. Interface Anal.* **1989**, *14* (3), 121−131.
(90) Wehrens-Dijksma, M.; Notten, P. H. L. *Electrochim. Acta* **2006**, *51* (18), 3609−3621.
(91) Gonzalezelipe, A. R.; Holgado, J. P.; Alvarez, R.; Munuera, G. *J. Phys. Chem.* **1992**, *96* (7), 3080−3086.
(92) Langell, M. A. *Surf. Sci.* **1987**, *186* (1−2), 323−338.
(93) Wulser, K. W.; Langell, M. A. *Surf. Sci.* **1994**, *314* (3), 385−397.
(94) Greiner, M. T.; Helander, M. G.; Wang, Z. B.; Tang, W. M.; Lu, Z. H. *J. Phys. Chem. C* **2010**, *114* (46), 19777−19781.
(95) Cahen, D.; Kahn, A. *Adv. Mater.* **2003**, *15* (4), 271−277.
(96) Ishii, H.; Sugiyama, K.; Ito, E.; Seki, K. *Adv. Mater.* **1999**, *11* (12), 972−972.
(97) Ishii, H.; Sugiyama, K.; Ito, E.; Seki, K. *Adv. Mater.* **1999**, *11* (8), 605−+.
(98) Gorschluter, A.; Merz, H. *Phys. Rev. B* **1994**, *49* (24), 17293−17302.
(99) Hugel, J.; Belkhir, M. *Solid State Commun.* **1990**, *73* (2), 159−162.
(100) Kadossov, E. B.; Gaskell, K. J.; Langell, M. A. *J. Comput. Chem.* **2007**, *28* (7), 1240−1251.
(101) Brandow, B. H. *Adv. Phys.* **1977**, *26* (5), 651−808.
(102) Fujimori, A.; Minami, F. *Phys. Rev. B* **1984**, *30* (2), 957−971.
(103) McKay, J. M.; Henrich, V. E. *Phys. Rev. Lett.* **1984**, *53* (24), 2343.
(104) See, A. K.; Klebanoff, L. E. *J. Vac. Sci. Technol., A* **1995**, *13* (3), 1527−1530.

(105) Eberhardt, W.; Plummer, E. W. *Phys. Rev. B* **1980**, *21* (8), 3245−3255.
(106) Guillot, C.; Ballu, Y.; Paigne, J.; Lecante, J.; Jain, K. P.; Thiry, P.; Pinchaux, R.; Petroff, Y.; Falicov, L. M. *Phys. Rev. Lett.* **1977**, *39* (25), 1632−1635.
(107) Himpsel, F. J.; Heimann, P.; Eastman, D. E. *J. Appl. Phys.* **1981**, *52* (3), 1658−1663.
(108) Clauberg, R.; Gudat, W.; Radlik, W.; Braun, W. *Phys. Rev. B* **1985**, *31* (4), 1754−1758.
(109) Chu, C. C.; Best, P. E. *Phys. Rev. B* **1979**, *19* (7), 3414−3419.
(110) Mankey, G. J.; Willis, R. F.; Himpsel, F. J. *Phys. Rev. B* **1993**, *48* (14), 10284−10291.
(111) Speier, W.; Zeller, R.; Fuggle, J. C. *Phys. Rev. B* **1985**, *32* (6), 3597−3603.
(112) Turtle, R. R.; Liefeld, R. J. *Phys. Rev. B* **1973**, *7* (8), 3411−3419.
(113) Goldmann, A.; Donath, M.; Altmann, W.; Dose, V. *Phys. Rev. B* **1985**, *32* (2), 837−850.
(114) Van der Ven, A.; Morgan, D.; Meng, Y. S.; Cederc, G. *J. Electrochem. Soc.* **2006**, *153* (2), A210−A215.
(115) Barde, F.; Palacin, M. R.; Chabre, Y.; Isnard, O.; Tarascon, J. M. *Chem. Mater.* **2004**, *16* (20), 3936−3948.
(116) Oliva, P.; Leonardi, J.; Laurent, J. F.; Delmas, C.; Braconnier, J. J.; Figlarz, M.; Fievet, F.; Deguibert, A. *J. Power Sources* **1982**, *8* (2−3), 229−255.
(117) Guan, Z. L.; Kim, J. B.; Wang, H.; Jaye, C.; Fischer, D. A.; Loo, Y. L.; Kahn, A. *Org. Electron.* **2010**, *11* (11), 1779−1785.
(118) Braun, S.; Salaneck, W. R.; Fahlman, M. *Adv. Mater.* **2009**, *21* (14−15), 1450−1472.
(119) Fahlman, M.; Crispin, A.; Crispin, X.; Henze, S. K. M.; de Jong, M. P.; Osikowicz, W.; Tengstedt, C.; Salaneck, W. R. *J. Phys.: Condens. Matter* **2007**, *19* (18), No. 183202.
(120) Tengstedt, C.; Osikowicz, W.; Salaneck, W. R.; Parker, I. D.; Hsu, C. H.; Fahlman, M. *Appl. Phys. Lett.* **2006**, *88* (5), No. 053502.
(121) Xu, Z.; Chen, L. M.; Chen, M. H.; Li, G.; Yang, Y. *Appl. Phys. Lett.* **2009**, *95* (1), No. 013301.